Effects of spin-orbit interaction in chromium on oxygen K-edge x-ray magnetic circular dichroism spectra in CrO_2

Akihiro Koide and Toshihiko Yokoyama
Department of Materials Molecular Science, Institute for Molecular Science, Myodiji-cho, Okazaki, 444-8585, Japan
(Received 19 June 2017; revised manuscript received 16 September 2017; published 17 October 2017)

We calculate the oxygen K-edge x-ray magnetic circular dichroism (XMCD) spectra of CrO_2 to investigate the origin of light-element XMCD. The XMCD spectra evaluated by using a multiple scattering theory are interpreted in terms of the spin-orbit interaction (SOI) at each atomic site. We find that the SOI at the nearest-neighbor Cr atoms dominantly contributes to the oxygen K-edge XMCD. Since it has been speculated that XMCD originates from the spin polarization and the SOI at the x-ray-absorbing atom, the present finding may lead to modification of the previously speculated mechanism underlying K-edge XMCD. We also perform calculations with a small CrO_2 cluster to examine how the O-p and Cr-d states are hybridized and how oxygen atoms acquire orbital angular momentum density. Strong K-edge XMCD features reflect the character of the d states of neighboring magnetic atoms and do not directly connect to the orbital magnetic moments of light-element p states.

DOI: 10.1103/PhysRevB.96.144419

I. INTRODUCTION

X-ray magnetic circular dichroism (XMCD) is a powerful tool to study the local magnetic structures of atoms owing to its element and orbital selectivity with regard to x-ray absorption. The sum rules for $L_{2,3}$- and $M_{4,5}$-edge XMCD separately afford the orbital and effective spin moments for an x-ray-absorbing atom [1–4]. This formalism has prompted the application of XMCD to various magnetic materials containing transition metals (TMs) and/or rare-earth elements to probe the local moments of d and f electrons. On the other hand, the sum rule for K-edge XMCD can be used to detect p-orbital moments; however, it has hardly been applied to practical cases because the number of valence p holes cannot be clearly estimated from the x-ray absorption spectra (XAS) [5,6]. Historically, K-edge XMCD spectra for pure TMs were the focus of theoretical XMCD studies because of their simple electronic and geometric structures [5–12]. Practically, K-edge XMCD measurements of TM compounds afford several advantages since hard x-ray experiments allow us to investigate magnetic properties in atmospheric and high-pressure conditions, although the orbital selectivity may play no important role in these cases [13,14]. The K-edge XMCD spectra of light elements, wherein their p orbitals essentially contribute to the physical properties, can elucidate magnetic structures mediated by light elements. The oxygen K-edge XMCD of $La_{1-x}Sr_xMnO_{3+\delta}$ has been utilized to clarify the mechanism of the metal insulator transition mediated by oxygen atoms [15]. Further, the oxygen K-edge XMCD of CrO_2 has been used to explicitly demonstrate the hybridization of Cr $3d$ and O $2p$ states and the delocalized properties of the hybridized states [16,17]. In addition, the nitrogen K-edge XMCD of ferromagnetic GdN has yielded information on magnetically polarized unoccupied $2p$ states; GdN exhibits giant magnetic resistance and a phase transition from metal (low temperature) to insulator (high temperature) at its Curie temperature [18,19]. For graphene on Ni(111), which was theoretically predicted as a spin filter [20], the carbon K-edge XMCD demonstrated a strong signal at the π^* peak, which may be related to spin polarization on carbon [21,22]. Thus the investigation of local magnetization in light elements by XMCD has played an important role in understanding various physical properties in terms of the hybridizations between light elements and magnetic atoms.

The origin of XMCD is different between the $L_{2,3}$ and K edges. In essence, XMCD arises from the spin-orbit interaction (SOI), which connects the spin and angular momenta between the core electron and incident circularly polarized x rays. For the $L_{2,3}$ edge with delocalized unoccupied d states, the core $2p$ states have orbital angular momenta and strong SOI due to their large binding energies, thus leading to the splitting of the $2p$ states into the $2p_{1/2}$ and $2p_{3/2}$ levels. The large core SOI yields substantial $L_{2,3}$-edge XMCD corresponding to several tens of percent of the x-ray absorption intensity. The orbital magnetic moment, which appears through the SOI in the valence bands, is not essential to provide large XMCD, although it contributes to the deviation of the L_3/L_2 ratio from -1. On the other hand, the core s states exhibit no SOI because of the absence of the orbital angular momentum. The SOI on unoccupied p states at the absorbing atom is essentially important to yield the K-edge XMCD intensity. This means that the unoccupied p states, to which the core electron is excited, should have orbital polarization. However, the SOI at light elements is generally fairly weak because of the weak gradient of Coulomb potentials when compared with that of heavier elements. In addition, light elements are usually nonmagnetic, and their spin and orbital polarizations could be very small. In spite of the small spin and orbital polarizations, the observed K-edge XMCD of light elements was found to be around 100 times larger than that of pure TMs [5,6,16]. In the context of the sum rule analysis for $L_{2,3}$-edge XMCD, the SOI at the x-ray-absorbing atom can be attributed to strong XMCD signals. Thus there is an apparent contradiction between the small SOI and the observed strong XMCD signals.

Theoretical studies on K-edge x-ray absorption spectroscopy (XAS) have been performed using real-space multiple scattering (MS) theories [23,24], which correspond to the Fourier transformation of the Korringa-Kohn-Rostoker (KKR) method [25]. In this regard, Ebert *et al.* developed the full relativistic KKR method [8], while Brouder *et al.* exploited the MS K-edge XMCD theory for powder samples [9]. Further, Fujikawa *et al.* developed the MS theory with

arbitrary incident x-ray directions [10,11]. Recently, Koide has studied the SOI effects at the surrounding atoms by modifying the MS theory [12]. Igarashi and Hirai have studied the effects of $4p$ and $3d$ SOI on pure TM K-edge XMCD spectra using the tight-binding approach [5,6]. They found that the $3d$ SOI dominantly contributes to the K-edge XMCD spectra and that p–d hybridization is important to generate the density of the $4p$ orbital angular momentum. However, it is ambiguous as to which SOI in the x-ray-absorbing or neighboring atoms is crucial. For light-element XMCD, the situation is in principle fairly clear, but there has been no report on this topic to the best of our knowledge. From the viewpoint of first-principles calculations, light-element XMCD is a challenging topic because of the importance of electron correlation. Solids composed of purely s and p electrons, which are weakly correlated, rarely show ferromagnetism. Light-element compounds with magnetic atoms are often classified with strongly correlated systems such as NiO, CoO, Fe_3O_4, and CrO_2, and simple reference magnetic systems composed of light elements are hardly observed. Nevertheless, the XAS of light elements has been often compared with the local densities of states (LDOS) with p symmetry of the absorbing atom in the ground electronic states [17,19,26,27]. The agreement between the two data sets has been found to be satisfactory, and this has allowed researchers to discuss the relationship between the crystal structure and observed XAS features [26,27].

As a reference of the ferromagnetic light-element compounds, we focus on CrO_2 to investigate light-element XMCD. CrO_2 has been known as a half metallic ferromagnet, where a majority (minority) spin act as metallic (semiconductor or insulator); in other words, a perfect spin-polarized current is constructed by majority spin electrons. CrO_2 has attracted attention as a promising candidate for spintronic devices which utilize electronic charge and spin degrees of freedom. The mechanism of the half metallicity in CrO_2 has been roughly understood by the double exchange scheme, where localized and delocalized d electrons on Cr^{4+} have exchange interaction with each other [28,29]. Another mechanism has been proposed that the majority and minority band structures in CrO_2 take similar structures in TiO_2 and RuO_2, respectively, to minimize the total electronic energy of CrO_2 [30]. The half metallic property was experimentally proved by the point contact Andreev reflection measurement [31] and bulk-sensitive x-ray photoemission spectroscopy [32,33]. Theoretical studies also predicted the half metallicity of CrO_2 [27–30,34–36]. Combining the electron correlation parameter U with the local-density approximation (LDA), the spin magnetic moment on a Cr ion was correctly calculated [37,38]. In more detailed discussion, however, the electron correlation in CrO_2 is controversial: no need of the parameter U was indicated by the Kerr effect measurements [35,39], while the dynamical mean field theory, which is one of the state-of-art approximations beyond using the Hubbard U, has not triumphed over the LDA+U for the magnetism of CrO_2 [32,36,40]. Nevertheless, when we avoid a much detailed problem, because of the itinerant electronic property, the electron correlation in CrO_2 may be moderate compared with a more localized electronic system such as NiO. Indeed, calculations based on density functional theory (DFT) without U also show half metallic band structures of CrO_2 [27,34,35]. The mild electron correlation therefore could allow us to use one-electron approaches [17,19,26,27]. This is why we choose the oxygen K edge ($1s \rightarrow np$) of CrO_2 to demonstrate the mechanism of K-edge XMCD.

In the present paper, we introduce the MS theory including the SOI in surrounding atoms for the calculations of XMCD spectra. Using the MS theory, we find that the SOI at the absorbing O atom has negligible contribution, whereas the one at the nearest Cr atoms is dominant to the XMCD spectra of CrO_2. Comparing the x-ray absorption and XMCD spectra with O-p local density of states (LDOS) and orbital angular momentum density, respectively, shows the importance of hybridization between O-p and Cr-d states. We also analyze the case of a diatomic CrO system to understand the origin of K-edge XMCD more clearly. A modified mechanism of K-edge XMCD is proposed, emphasizing the difference from the case of $L_{2,3}$ edge.

II. THEORY

In the previous work [12], we briefly reviewed the MS theory including the SOI in the surrounding atoms for XMCD. Here, we discuss the MS theory in further detail. The absorption intensity $I(\omega,m_p)$ for incident photon energy ω with the helicity ($m_p = \pm 1$) of circularly polarized x rays can be expressed as [11]

$$I(\omega,m_p) = -2\,\mathrm{Im}\langle c|H_{ep}^{\dagger}(m_p)g_D(\varepsilon)H_{ep}(m_p)|c\rangle \quad (1)$$

$$= T_{11}(\omega,m_p) + T_{12}(\omega,m_p) + T_{21}(\omega,m_p) + U_{11}(\omega,m_p) + \cdots, \quad (2)$$

$$\varepsilon = \omega + \varepsilon_{\mathrm{core}} - E_0. \quad (3)$$

Here, $g_D(\varepsilon)$ represents the one-electron Dirac Green's function with photoelectron energy ε measured from E_0. The threshold energy E_0 is not necessarily consistent with the vacuum level. One may choose the average of the Coulomb potentials at atomic site boundaries as E_0. The electron-photon interaction $H_{ep}(m_p)$ with photon helicity m_p operates the ket of the 4-spinor core orbital $|c\rangle$, which is composed by two 2-spinors $|\varphi_c\rangle$ and $|\chi_c\rangle$. The one of the 2-spinors $|\varphi_c\rangle$ corresponds to the nonrelativistic limit of a solution of Dirac equation with a central force potential. When relativistic effects become larger, $|\chi_c\rangle$ has more contribution to the solution. The correlated nonrelativistic Green's function $g(\varepsilon)$ can expand $g_D(\varepsilon)$ [9,11,41], and the expansion yields T_{11}, T_{12}, T_{21}, and U_{11}. The Green's function is expressed as

$$g(\varepsilon) = \frac{1}{\varepsilon - H + i\eta} \quad (\eta \rightarrow +0), \quad (4)$$

$$H = T + V - E_0, \quad (5)$$

$$V - E_0 \sim \sum_{\alpha} v_{\alpha} - i\Gamma. \quad (6)$$

The effective total potential $V - E_0$ for an excited electron can be separated into each atomic-site contribution v and the imaginary part describing the photoelectron damping by inelastic scatterings. The expanded term of $I(\omega,m_p)$ corresponding to the nonrelativistic limit is denoted by T_{11},

written as

$$T_{11}(\omega,m_p) = -2\,\mathrm{Im}\langle\varphi_c|\Delta^*_{m_p} g(\varepsilon)\Delta_{m_p}|\varphi_c\rangle. \quad (7)$$

The 2-spinor $|\varphi_c\rangle$ is influenced by the electron-photon interaction operator Δ_{m_p} in the 2-spinor form. In the dipole approximation, the operator is written by $\Delta_{m_p} \sim rY_{1m_p}$ in the length representation. Although the term T_{11} corresponds to the strongest intensity among the four terms for XAS, it does not contribute to the K-edge XMCD intensity because the $1s_{1/2}$ core state has no SOI. The intensities T_{12} and T_{21} reflect the relativistic effects only on the absorbing atom. Their details are shown in Ref. [11]. The most important term as regards XMCD in the expanded terms in U_{11} includes SOI δV for the photoelectron state:

$$U_{11}(\omega,m_p) = -2\,\mathrm{Im}\langle\varphi_c|\Delta^*_{m_p} g(\varepsilon)\delta V g(\varepsilon)\Delta_{m_p}|\varphi_c\rangle. \quad (8)$$

The total SOI δV can be separated into the SOIs at each site δv, similar to the total potential V:

$$\delta V = \sum_\alpha \delta v_\alpha, \quad (9)$$

$$\delta v = \xi\sigma\cdot\mathbf{L}, \quad (10)$$

$$\xi = \frac{1}{4c^2}\frac{1}{r}\frac{dv}{dr}, \quad (11)$$

where $\mathbf{L}$ is the angular momentum operator and σ the Pauli matrix. This allows us to derive a MS expansion for U_{11}.

The damping free propagator g_0 with damping factor Γ and site T-matrix t are introduced as

$$g_0 = \frac{1}{\varepsilon - T + i\Gamma}, \quad (12)$$

$$t_\alpha = v_\alpha + v_\alpha g_0 t_\alpha. \quad (13)$$

The site T-matrix t_α fully describes photoelectron scattering in the α site without the SOI. In addition, propagator g_α, fully including the site potential v_α, is written as

$$g_\alpha = g_0 + g_0 t_\alpha g_0 = \frac{1}{\varepsilon - T - v_\alpha + i\Gamma}. \quad (14)$$

Thus, with the use of the above formulas, the MS expansion of $g(\varepsilon)$ can be expressed as

$$g = g_A + \sum_{\alpha(\neq A)} g_A t_\alpha g_A + \sum_{\beta(\neq\alpha,A)}\sum_{\alpha(\neq A)} g_A t_\beta g_0 t_\alpha g_A + \cdots \quad (15)$$

$$\equiv g_A + g^{sc}_{AA} \quad (16)$$

$$= g_B v_B g_A + g_A + \sum_{\alpha(\neq A,B)} g_B t_\alpha g_A + \sum_{\beta(\neq\alpha,B)}\sum_{\alpha(\neq A)} g_B t_\beta g_0 t_\alpha g_A + \cdots \quad (17)$$

$$\equiv g_{BA} + g^{sc}_{BA} \quad (A \neq B), \quad (18)$$

where sites A and B represent the x-ray-absorbing and photoelectron-scattering atomic sites, respectively.

Using the MS expansion, we classify U_{11} into atomic and scattering SOI terms as U^A_{11} and U^{sc}_{11}, respectively:

$$U_{11} = U^A_{11} + U^{sc}_{11}, \quad (19)$$

$$U^A_{11} = -2\,\mathrm{Im}\langle\varphi_c|\Delta^*\big(g_A\delta v_A g_A + g^{sc}_{AA}\delta v_A g_A + g_A\delta v_A g^{sc}_{AA}\big)\Delta|\varphi_c\rangle, \quad (20)$$

$$U^{sc}_{11} = -2\,\mathrm{Im}\sum_{B(\neq A)}\langle\varphi_c|\Delta^*\big(g_{AB}\delta v_B g_{BA} + g^{sc}_{AB}\delta v_B g_{BA} + g_{BA}\delta v_B g^{sc}_{BA}\big)\Delta|\varphi_c\rangle - 2\,\mathrm{Im}\sum_\alpha\langle\varphi_c|\Delta^* g^{sc}_{A\alpha}\delta v_\alpha g^{sc}_{\alpha A}\Delta|\varphi_c\rangle. \quad (21)$$

It should be noted that the last term in U^{sc}_{11} includes the SOI at A in a photoelectron MS process. Intensity $U_{11,A}$ includes the SOI at site A in nonscattering processes. The photoelectron is influenced by δv_A when it initially moves out from or finally returns to site A. In combination with T_{12} and T_{21}, the XMCD intensity ΔI^A without the SOI scattering can be defined as

$$\Delta I^A = \big[T_{12} + T_{21} + U^A_{11}\big]_{m_p=+1} - \big[T_{12} + T_{21} + U^A_{11}\big]_{m_p=-1}. \quad (22)$$

This contribution has been numerically studied by Fujikawa [10,11].

In summary, the total XAS and XMCD intensity I and ΔI are obtained as

$$I = T_{11}(+) + T_{11}(-), \quad (23)$$

$$\Delta I = \Delta I^A + \Delta I^{sc}, \quad (24)$$

$$\Delta I^{sc} = U^{sc}_{11}(+) - U^{sc}_{11}(-). \quad (25)$$

A more explicit form of U^{sc}_{11} is derived in the Appendix.

By using one-electron Green's functions without the damping factor, we can also obtain the one-electron density of states:

$$D(\varepsilon) = \sum_i D_i(\varepsilon) = \sum_i\int_{\Omega_i} d\mathbf{r}_i\,\mathcal{D}(\mathbf{r}_i;\varepsilon), \quad (26)$$

$$\mathcal{D}(\mathbf{r};\varepsilon) = -\frac{1}{\pi}\mathrm{Im}\langle\mathbf{r}|g_D(\varepsilon)|\mathbf{r}\rangle \sim \mathcal{D}_{11} + \mathcal{D}_{12} + \mathcal{D}_{21} + \mathcal{D}'_{11} \sim \mathcal{D}_{11} + \mathcal{D}'_{11}. \quad (27)$$

In our MS calculation, region Ω_i represents the atomic sphere at site i. We assume that the contribution of the interstitial region and overlap between atomic spheres are small. The energy-dependent charge density $\mathcal{D}$ can be expanded in the same way as the x-ray absorption intensity I in Eqs. (1) and (2). For the relativistic correction, we only take $\mathcal{D}'_{11}$ into account to include the SOI effect. Since the expressions of $\mathcal{D}_{11}$ and $\mathcal{D}'_{11}$ resemble those of T_{11} and U_{11}, respectively, further derivation of $\mathcal{D}$ can proceed in a similar manner.

III. METHOD

The effective self-consistent single-particle potentials for MS calculations were obtained in the LDA using the linear-muffin-tin-orbital (LMTO) method [42]. In our study, we

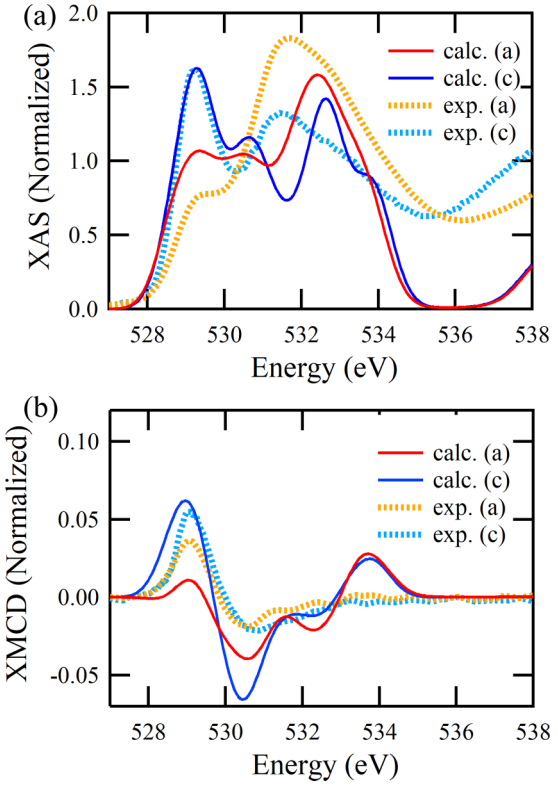

FIG. 1. Calculated angular-dependent oxygen K-edge (a) XAS and (b) XMCD spectra of CrO_2. Incident x-ray directions along the crystal a and c axes of CrO_2 are denoted by (a) and (c). For comparison, experimental spectra are also shown [16].

used space-filled (and partially overlapping) atomic spheres. In these self-consistent calculations, SOI was not taken into account. Although the densities of states and magnetic moments are influenced by the Hubbard U parameter of 3.0 eV within the LDA + U scheme, the value of which is widely adopted for CrO_2 [29,34,37,38], the charge density and effective potentials do not vary significantly. The XAS and XMCD were calculated using a spherical cluster of 359 atomic sites including 196 empty spheres. The cluster has the rutile structure of CrO_2 with the cell parameters of $a = b = 4.421$ Å and $c = 2.916$ Å determined experimentally [43]. The calculated XAS and XMCD were convoluted by Gaussian functions with half widths at half maximum of 0.5 eV in order to simulate finite natural widths and experimental resolution. In our MS calculation, the photoelectron damping factor was not employed, thereby resulting in not complex but real photoelectron energies, to interpret XAS and XMCD by LDOS and the density of orbital angular momenta. We did not observe any singularity in the calculations arising from the use of the real energies, as discussed in Ref. [9]. The calculated angle-resolved spectra were obtained with the incident x-ray directions lying perfectly along the a and c axes of CrO_2.

IV. RESULTS AND DISCUSSION

Figures 1(a) and 1(b) show calculated angle-resolved oxygen K-edge XAS and XMCD spectra of CrO_2, respectively; the experimental spectra are also shown for comparison [16]. The calculated XAS for the c-axis-incident x rays was normalized with the first peak intensity to fit the experimental spectrum. This normalization constant was applied to the other calculated XAS and XMCD spectra. In Fig. 1(a), the calculated angular dependence at ~529 and 532 eV agrees well with the experimental one. The calculated peak at 530.5 eV in XAS may correspond to the experimental peak at 531.5 eV. This deviation between experiment and calculation may arise due to the absence of the U correction in our MS calculations. The calculated spin-dependent LDOS of CrO_2 with various U parameters showed that the unoccupied minor spin LDOS is shifted up from the Fermi level (E_F), which may improve the correspondence of O-p LDOS to the oxygen K-edge XAS [27,34]. In addition, our calculations do not include energy-dependent broadening originating from the imaginary part of the self-energy, which describes the photoelectron inelastic mean free path. The smaller calculated intensity may be improved by such energy-dependent broadening effects. Here, we note that this small intensity has also been observed in the calculated XAS based on the full-potential LMTO (FPLMTO) method [17]. In Fig. 1(b), the calculated XMCD peak at 529 eV and its angular dependence show good agreement with the corresponding experimental values. The discrepancy in the higher-energy side may also be caused by the absence of the U correction. The larger XMCD signals at 530.5 and 532.8 eV in the calculated spectra exhibit the same trend as the FPLMTO result [17]. The full-potential MS theory [44,45] may work to improve our calculated results; at present, however, the spin-dependent XMCD calculations have not been implemented in the code. Although there might be other important factors to describe better electronic structures, we avoid detailed discussion because the most plausible way has not yet been settled [32,36,40].

To study the origin of the oxygen K-edge XMCD intensity, we separate the intensity contributions to the XMCD spectra in terms of each site SOI. These results are shown in Figs. 2(a) and 2(b). Obviously, the contributions of the SOI at the x-ray-absorbing atom (ΔI^A) are significantly smaller than those of the experimental spectra. The phases of the oscillation in ΔI^A are also different from the experimental one. This result indicates the limitation of the MS calculations only including the SOI at the x-ray-absorbing site for XMCD, and it is consistent with the physical intuition that light elements have negligibly small SOI. On the other hand, the sum of the first nearest-neighbor Cr contributions (ΔI^{sc} for $Cr^{(1)}$) is almost equivalent to the spectra in total (ΔI). Therefore, we conclude that the origin of strong oxygen K-edge XMCD in CrO_2 is the SOI at the Cr atoms neighboring to the x-ray-absorbing oxygen atom. The small difference between ΔI and ΔI^{sc} for $Cr^{(1)}$ is attributed to the contributions from the other ΔI^{sc}. Here, we note that the decomposition of XMCD by the site SOI may be easier than that by scattering paths, whose number is obviously greater than the number of sites. Moreover, the path expansion for effective potential (or site T matrix) within a finite MS scheme, instead of infinite scattering calculation, does not always converge in the energy region of XMCD [46]. In our calculation, we adopt the infinite scattering scheme for the effective potential, as expressed in Eq. (A13). Therefore, the site-resolved scheme using the SOI is more useful to interpret the XMCD spectra.

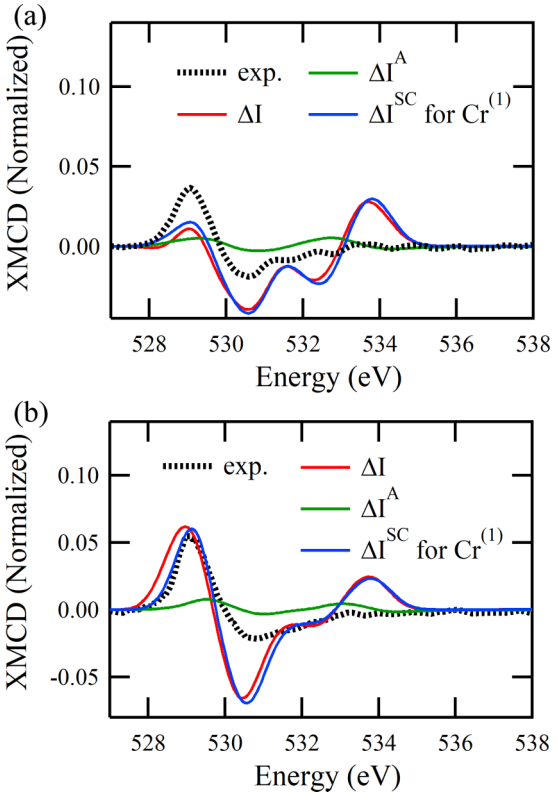

FIG. 2. Calculated oxygen K-edge XMCD spectra with incident x rays parallel to the (a) a and (b) c axes of CrO_2. Each term is represented in Eq. (24). The experimental spectra and ΔI are also indicated, similar to those in Fig. 1(b). The contribution from the first nearest-neighbor Cr atoms ($Cr^{(1)}$) shows the sum of the contributions from three nearest-neighbor $Cr^{(1)}$ atoms around the x-ray-absorbing oxygen atom.

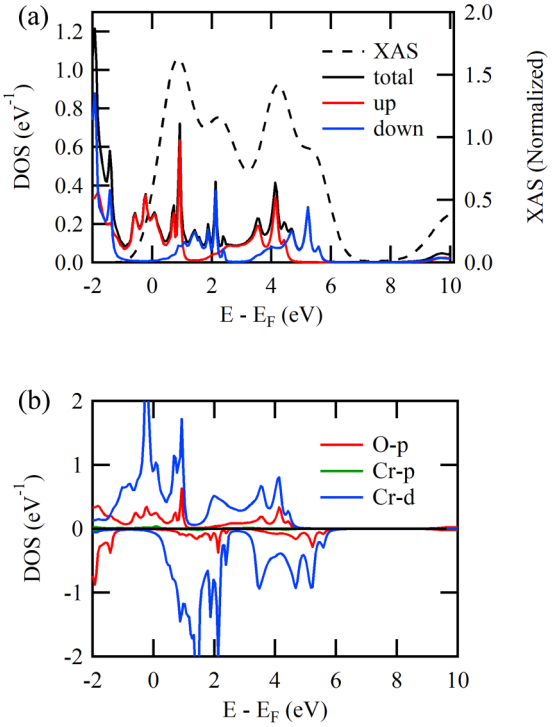

FIG. 3. (a) Calculated O-p LDOS for CrO_2 compared with the XAS denoted by the calc. (c) in Fig. 1(a). For the O-p LDOS, spin-dependent components are shown. (b) Calculated spin-resolved LDOSs of O-p, Cr-p, and Cr-d. The negative value shows the density for minority (down) spin. The Cr-p LDOS is negligibly small compared with other components.

Figure 3(a) shows the oxygen K-edge XAS and O-p LDOS obtained by summing the components of $m = +1$ and -1. The XAS agrees well with the total LDOS. Therefore, we can conclude that LDOS is useful and widely applicable for the interpretation of XAS when the single-particle description is valid [26,27]. The peaks at about 1 and 4 eV (2 and 5 eV) are attributed to the up (down) spin component of the O-p LDOS. Figure 3(b) shows calculated spin-resolved LDOSs of O-p, Cr-p, and Cr-d for CrO_2. Hereafter we define up (down) spin as majority (minority) spin. The half-metallic electronic structure is successfully obtained. One can see hybridization of O-p states with Cr-d, but not Cr-p which is negligible. Since the crystal structure of CrO_2 is that of rutile with a Cr ion in a distorted octahedron with nearest neighbor O ions, the Cr-d LDOS structure and its hybridized components have been interpreted by t_{2g} and e_g bands as in the literature [27,28,30]. In our calculated XAS in Fig. 3(a), the first (second) pair of a peak and a shoulder corresponds to the t_{2g} (e_g) component. As mentioned in the discussion about Fig. 1(a), the Hubbard U may push up the down-spin band. Therefore, the first and second structures in the experimental XAS may be assigned by majority spin t_{2g} and the others, respectively [27]. It is noted that, in the dipole approximation and the one-particle picture, the K-edge x-ray absorption may correspond to the optical transition from the core 1s to the unoccupied p states at the origin of the absorbing atom because of the extremely localized 1s wave function. In addition, for example, when the Cr-d wave function is reexpanded at a different origin such as at an oxygen site, it has p components at the new origin. This is why the O-p LDOS and the hybridization with the Cr-d state are important.

Figure 4(a) shows the LDOS difference (total) between the O-p ($m = \pm 1$) orbitals, together with the XMCD of the calc. (c) in Fig. 1(b). The LDOS differences of the O-p ($m = \pm 1$) orbitals with respect to the LDOSs without the SOI are also depicted. The XMCD and the total term exhibit the same energy dependence. This can be expected from Fig. 3(a), wherein the XAS is consistent with the sum of the LDOS with $m = \pm 1$. Since XAS (XMCD) data are defined by the sum (difference) of the x-ray absorption with circularly polarized x rays of positive and negative helicities, XMCD corresponds to the difference between LDOS with $m = \pm 1$. In Fig. 4(a), the $m = \pm 1$ components of the LDOS deviation have the opposite sign and cancel each other. Since the spin index is summed up in LDOSs with $m = \pm 1$, the perturbed SOI causes energy shifts of LDOSs with $m = \pm 1$ in opposite directions, away from each other. These shifts eventually lead to the opposite signs of the LDOS differences. For example, the difference between a certain Gaussian function and one shifted by $\pm\Delta$ show the opposite sign when $\Delta \ll 1$ as a perturbation. Moreover, degenerate levels in the magnetic quantum numbers are split by the SOI, but the total number of the energy levels is conserved. The cancellation corresponds to the fact that the

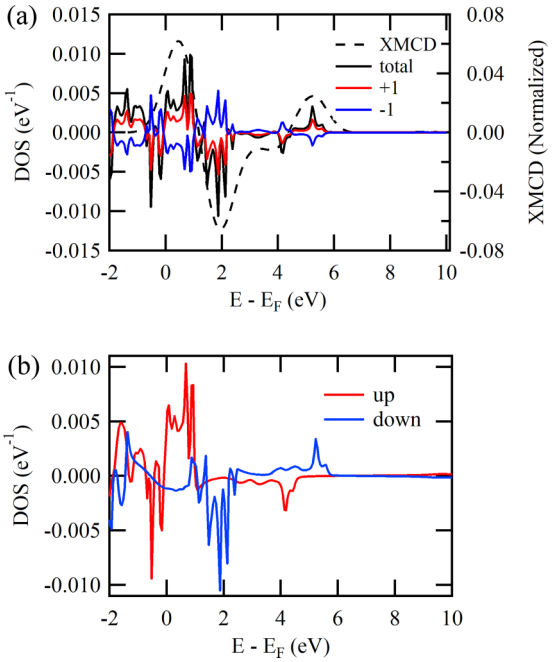

FIG. 4. (a) LDOS difference (total) between the O-p ($m = \pm 1$) orbitals for CrO_2. The LDOS differences of the O-p ($m = \pm 1$) orbitals with respect to the LDOSs without the SOI are also depicted. The XMCD spectrum of the calc. (c) in Fig. 1(b) is shown for comparison. (b) The total spin-resolved components.

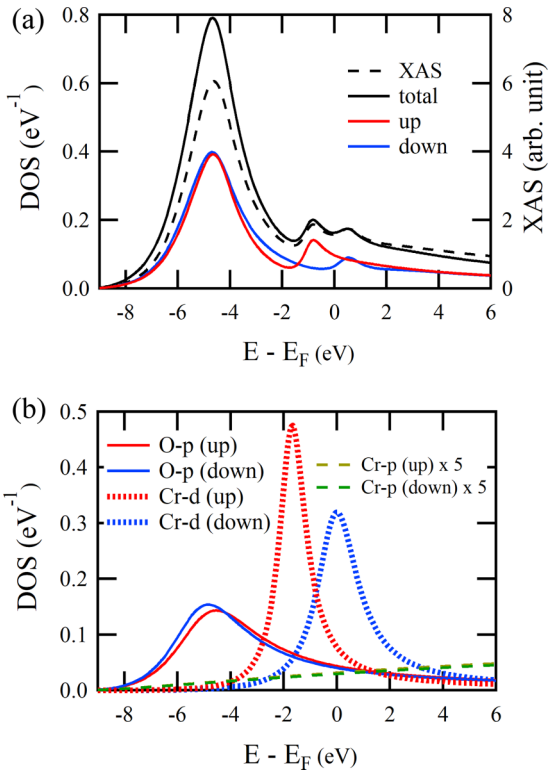

FIG. 5. Calculated oxygen K-edge XAS and O-p LDOS for (a) with and (b) without scattering contributions in the diatomic CrO system. For the LDOS, spin-dependent components are shown. Moreover, the spin-dependent no-scattering Cr-p and -d LDOSs are also depicted in Fig. 5(b). Here, we note that XAS below the Fermi level of CrO_2 is indicated hypothetically because of the absence of multiplication of the Fermi distribution function.

integration of the densities of the orbital angular momenta vanishes over the entire energy range. Thus the integral in the range for the unoccupied states is directly connected to that for the occupied state, which is the orbital magnetic moment. The sum rule for the orbital magnetic moment makes use of this relation [1,5,6]. The unoccupied orbital density is obtained from the integral of the strong XAS peak near the absorption threshold energy, which may be proportional to the number of valence holes. This procedure has been widely applied to $L_{2,3}$-edge XMCD of TM atoms [3,4]. However, for K-edge XMCD, it is difficult to separate the valence-hole contribution from the total XAS because the unoccupied p states are delocalized and merged with continuum states when compared with the TM d states [5,6]. In this context, Huang *et al.* obtained the O-p orbital magnetic moment from the oxygen K-edge XMCD of CrO_2 by using the sum rule [37]. Although the first XAS peak located at 529.2 eV in Fig. 3(a) is separated rather well from the subsequent broad structures in this spectra, the valence-hole contribution extracted should contain a large uncertainty of the determined orbital magnetic moments [37].

Figure 4(b) shows the spin-resolved components of the LDOS differences between the O-p ($m = \pm 1$) states for CrO_2. The first positive and negative XMCD peaks are attributed to the up- and down-spin components. From Figs. 3(b) and 4(b), the two peaks may be assigned to the t_{2g} states. Therefore, the hybridization between O-p and Cr-d states has the substantial contribution to the XMCD. In this calculation, the contribution of the SOI includes the crystal structural (band) effect by the infinite MS process, which cannot be separated into each MS path contribution for effective potential scattering [46]. Although the contribution of the SOI almost comes from the nearest neighbors as shown in Fig. 2, the hybridization may have farther contribution. The XMCD under only the hybridization between the absorbing oxygen atom and the nearest Cr atom may give the crucial origin of the XMCD. Hence we will restrict the hybridization without the other calculated conditions changed.

To understand the mechanism of the light-element XMCD more clearly, we calculated XAS and XMCD using a simple diatomic CrO molecule comprising x-ray-absorbing oxygen and nearest-neighbor Cr. The effective site potentials and E_F of CrO_2 were adopted for this minimal calculation. This procedure may suppress only the crystal structure effect but keep the other calculation conditions. Figure 5(a) shows the oxygen K-edge XAS and O-p LDOS in the same way as Fig. 3(a). In Fig. 5(a), the two small peaks near E_F of CrO_2 are decomposed by the up- and down-spin components. We also calculated the no-scattering contribution for LDOS, and the corresponding results are shown in Fig. 5(b). Because of the self-consistent effective site potentials of CrO_2, the no-scattering terms show their spin dependence, particularly the Cr-d atomic LDOSs. The small peaks in Fig. 5(a) appear due to the hybridization between the atomic Cr-d and tails of the atomic O-p LDOS. The Cr-p states have no importance. In addition, the atomic Cr-d (O-p) peaks shift to the higher

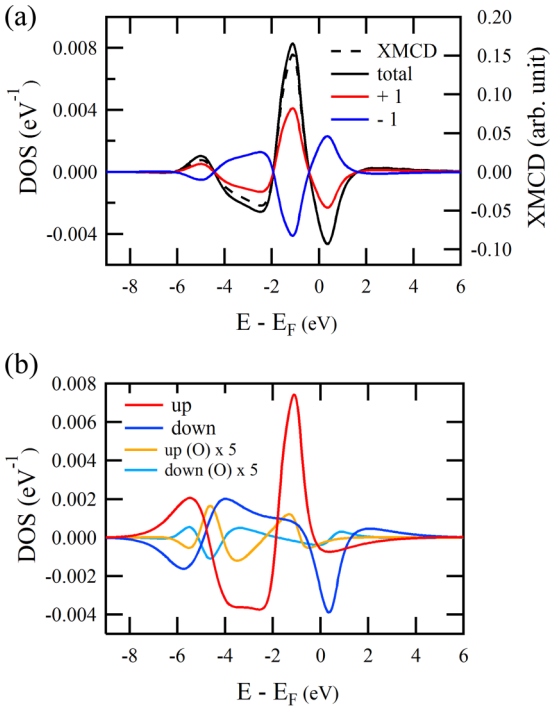

FIG. 6. (a) Calculated oxygen K-edge XMCD spectra and the LDOS difference (total) between the O-p ($m = \pm 1$) orbitals for the diatomic CrO system. The LDOS differences of the O-p ($m = \pm 1$) orbitals with respect to the LDOSs without the spin-orbit interaction (SOI) are also depicted. (b) The total spin-resolved components. XMCD below the Fermi level of CrO_2 is indicated hypothetically. Components only including the oxygen SOI are also shown.

(lower)-energy side in the O-p LDOS in Fig. 5(a). This result can be explained by the perturbation theory: when two states with a gap are hybridized, the gap size increases. In the calculation of bulk CrO_2, further hybridizations or MS processes promote the upward shift of the hybridized Cr-d states, thereby resulting in the half-metallic DOS with the up (down) spin component across (above) E_F of CrO_2 with complicated structures as shown in Figs. 3(a) and 3(b).

Figure 6(a) shows the LDOS differences (total) between the O-p ($m = \pm 1$) orbitals, together with the XMCD for the diatomic system. The LDOS differences of the O-p ($m = \pm 1$) orbitals with respect to the LDOSs without the SOI are also depicted. The XMCD and the total term exhibit the same energy dependence. In Fig. 6(a), the $m = \pm 1$ components of the LDOS difference have the opposite sign and cancel each other, similar to Fig. 4(a) for CrO_2. The other findings in Fig. 4(a) is also seen in Fig. 6(a).

Figure 6(b) shows the spin-resolved LDOS differences between the O-p ($m = \pm 1$) states for the diatomic CrO system. The peaks in the up and down components near E_F of CrO_2 originate from the hybridization with the Cr-d states or photoelectron scattering by the Cr atom, as shown in Fig. 5(b). Since the nonscattering component of the Cr-d LDOS is highly spin polarized, the orbital angular momentum is induced by its own SOI. Therefore, the Cr-d component appearing in the O-p LDOS due to hybridization should also exhibit orbital angular momenta. This explains why O-p states hybridized with the Cr-d state should have the density of the orbital angular momenta in spite of the small SOI present in an oxygen atom. This picture is different from the ones for $L_{2,3}$-edge XMCD of TMs, where the SOI is important only at the core $2p$ states in the x-ray-absorbing TM atom. The unoccupied states near E_F of CrO_2 strongly reflect the character of the magnetic Cr atoms. Thus the strong XMCD in Fig. 6(a) originates from the localized Cr-d character or the sharpness of the Cr-d LDOS. We note that the orbital magnetic moment does not directly correspond to the intensity of XMCD but is related to the integral of the XMCD spectrum. Even though the XMCD signals are strong, a Fano-line-shaped structure reduces its integral intensity and may provide a negligibly small orbital moment. When prominent XMCD features are observed, we can deduce that (i) the valence orbitals of magnetic atoms are strongly hybridized with those of the x-ray-absorbing light-element atom and (ii) the valence orbitals of magnetic atoms contain relatively localized and substantially spin-polarized d states. The highly spin-polarized d state deviates the densities of O-p ($m = \pm 1$) between the up and down spin components, and this may yield a clear XMCD structure. This scheme explains the stronger XMCD observed in the oxygen K edge of CrO_2 than those in the K edge of pure TMs [5,6].

Thus far, we have demonstrated the agreement of the calculations between the O-p LDOS and oxygen K-edge XAS. However, the situations for correlated systems including CrO_2 have been rather complicated. In the above discussion, we did not consider the core-hole effect. The negligible core-hole effect in the oxygen K-edge XAS of TM oxides has been addressed previously [26]. On the other hand, it has been reported that the core-hole effect should be taken into consideration in the interpretation of the oxygen K-edge XAS of α quartz [47]. Recently, Liang *et al.* demonstrated that the core-hole effect reduces the peak intensity of the oxygen K-edge spectra of TiO_2 and CrO_2, calculated within the single-particle description [48]. Since the O-p LDOS near E_F participates in the core-hole screening, the XAS intensity is strongly suppressed. Therefore, the ground state O-p LDOS without a core hole agrees rather well with the XAS. Liang *et al.* also showed that the reduced peak intensity revives upon many-electron excitations with a core hole [48]. This interpretation based on the many-body delta-self-consistent-field method agrees with the result of the Bethe-Salpeter-equation scheme, which describes the electron-hole pair beyond the one-body approach [49]. Qualitatively, the no-hole one-body calculations for the oxygen K-edge XAS of TM oxides may be easily addressed and prove useful.

V. CONCLUSION

We have calculated the contribution of each atomic-site SOI to the oxygen K-edge XMCD of CrO_2 by using the MS theory. Our calculated results have shown that oxygen K-edge XMCD of CrO_2 dominantly originates from the SOI in the nearest-neighbor Cr atoms, and not that in the x-ray-absorbing oxygen atom. Thus far, K-edge XMCD may be understood as the following description, similar to the $L_{2,3}$-edge cases: (i) O-p states are hybridized with Cr-d states; (ii) O-p states become spin polarized; (iii) O-p states become orbital polarized due to the polarized spin and its own SOI; (iv) oxygen K-edge

XMCD is observed. Here, we propose a corrected description as follows: (i′) Cr-d states are orbital polarized; (ii′) O-p states are hybridized with Cr-d states; (iii′) O-p states become spin and orbital polarized; (iv′) the oxygen K-edge XMCD is observed. The strong features observed in light-element K-edge XMCD are attributed to large localization, hybridization, and spin polarization of neighboring magnetic atoms. The orbital angular momenta can be qualitatively discussed via the integral of XMCD, and not by the peak intensity. The combination of XMCD analyses using the SOI at surrounding atoms with more accurate treatments such as full potential calculations and including electron-electron correlations and multielectron excitation processes will form our future work.

ACKNOWLEDGMENTS

This work was financially supported by a Grant-in-Aid for JSPS Fellows (Grant No. 15J07459) and by a Grant-in-Aid for Scientific Research (A) (Grant No. 15H02173). We would like to express our thanks to Prof. Peter Krüger of Chiba University for fruitful discussions and technical supports.

APPENDIX: DERIVATION OF U_{11}^{sc}

The explicit form of U_{11}^{sc} is derived here by using the MS expansion. For further calculations from the MS expansion, two-center expansion of the propagators at positions $\mathbf{r}'+\mathbf{R}_\beta$ and $\mathbf{r}+\mathbf{R}_\alpha$ can be used

$$g_0(\mathbf{r}'+\mathbf{R}_\beta,\mathbf{r}+\mathbf{R}_\alpha)=2\sum_{L'L} i^{l'-l}G^{\beta\alpha}_{L'L}(k)j_l(kr')Y_{L'}(\hat{\mathbf{r}}') \times j_l(kr)Y^*_L(\hat{\mathbf{r}})(\alpha\neq\beta) \quad (A1)$$

$$=-2ik\sum_L j_l(kr_<)h_l^{(1)}(kr_>)Y_L(\hat{\mathbf{r}}')Y^*_L(\hat{\mathbf{r}})(\alpha=\beta), \quad (A2)$$

$$g_\gamma(\mathbf{r}'+\mathbf{R}_\beta,\mathbf{r}+\mathbf{R}_\alpha)=2\sum_{L'L} i^{l'-l}G^{\beta\alpha}_{L'L}(k)R_l(kr')Y_{L'}(\hat{\mathbf{r}}') \times j_l(kr)Y^*_L(\hat{\mathbf{r}})(\gamma=\beta) \quad (A3)$$

$$=2\sum_{L'L} i^{l'-l}G^{\beta\alpha}_{L'L}(k)j_l(kr')Y_{L'}(\hat{\mathbf{r}}')R_l(kr)Y^*_L(\hat{\mathbf{r}})(\gamma=\alpha) \quad (A4)$$

$$=-2ik\sum_L R_l(kr_<)\bar{R}_l(kr_>)Y_L(\hat{\mathbf{r}}')Y^*_L(\hat{\mathbf{r}})(\gamma=\alpha=\beta), \quad (A5)$$

where photoelectron wave number $k=\sqrt{2(\varepsilon+i\Gamma)}$. Expansion coefficient $G^{\beta\alpha}_{L'L}(k)$ is known as the KKR structural factor, purely reflecting the local geometries of the systems [45]. In the above expression, we assume that v is spherical. The inner site vectors $\mathbf{r}'$ and $\mathbf{r}$ have their origins at $\mathbf{R}_\beta$ and $\mathbf{R}_\alpha$ for sites β and α, respectively. The wave functions j_l, $h_l^{(1)}$, R_l, and $\bar{R}_l$ with a partial wave l are the spherical Bessel function, spherical Hankel function of the first kind, and the regular and irregular solutions of the radial Schrödinger equation, respectively. Moreover, the site T matrix arising from a spherical site potential can be represented in the partial wave expansion, and it is related to phase shift δ as

$$t(\mathbf{r},\mathbf{r}')=\sum_L t_l(r,r')Y_L(\hat{r})Y^*_L(\hat{r}'), \quad (A6)$$

$$t_l(k)\equiv 2\int dr\,dr'r^2r'^2 j_l(kr)t_l(r,r')j_l(kr') \quad (A7)$$

$$=-\frac{e^{2i\delta_l}-1}{2ik}. \quad (A8)$$

If we use the MS expansion $g=g_{AA}+g^{sc}_{AA}$, the use of scattering-site terms such as $[g_A]\delta v_B[g_At_Bg_A]$ may lead to numerical problems because δv_B and t_B cannot be separated in the integral due to the expression of $g_A\sim g_0$ in Eq. (A2). Since it is difficult to obtain $t_l(r,r')$ directly, the separation of t in an integral and making use of $t_l(k)$ are important. In the MS expansion $g=g_{AB}+g^{sc}_{AB}$ in Eq. (18), the above example may correspond to $[g_B]\delta v_B[g_Bt_\alpha g_A]$, where δv and t do not belong to the same atomic site. Since this allows separation of the integration including δv and t, the integral is given as the phase shift in Eq. (A8).

By using the above expressions, U_{11}^{sc} can be separated into three scattering terms:

$$U^{sc}_{11}(m_p)=-\frac{2}{\pi}\mathrm{Im}\sum_\sigma \rho_\sigma^2\left(u^{GG}_{m_p,\sigma}+u^{Z'G}_{m_p,\sigma}+u^{Z'Z'}_{m_p,\sigma}\right), \quad (A9)$$

$$u^{GG}_{m_p,\sigma}=\sum_{B(\neq A)}\sum_L \Xi^{GG}_{BL,\sigma}G^{AB}_{1m_p,L}G^{BA}_{L,1m_p}, \quad (A10)$$

$$u^{Z'G}_{m_p,\sigma}=\sum_{B(\neq A)}\sum_L \Xi^{Z'G}_{BL,\sigma} \times\left(Z'^{AB}_{1m_p,L}G^{BA}_{L,1m_p}+G^{AB}_{1m_p,L}Z'^{BA}_{L,1m_p}\right), \quad (A11)$$

$$u^{Z'Z'}_{m_p,\sigma}=\sum_\alpha\sum_L \Xi^{Z'Z'}_{\alpha L,\sigma}Z'^{A\alpha}_{1m_p,L}Z'^{\alpha A}_{L,1m_p}, \quad (A12)$$

where the spin index σ is $+$ $(-)$ for the up (down) spin of the photoelectron and ρ denotes the dipole radial integral. The intensity of the photoelectron scattering by δv is denoted by Ξ. The KKR structural factor $G^{BA}_{L,1m_p}$ describes direct migration of photoelectron from site A with angular momentum $(1,m_p)$ to site B with L. Thus the single scattering by the SOI δv is given by u^{GG}. The MS factor Z', defined as

$$Z'^{\beta\alpha}_{L',L}=[G^{-1}-t]^{\beta\alpha}_{L',L}-G^{\beta\alpha}_{L',L} =[GtG+GtGtG+\cdots]^{\beta\alpha}_{L',L}, \quad (A13)$$

describes the photoelectron migration with MS by t from single to infinite MSs. It is to be noted that $u^{Z'G}$ and $u^{Z'Z'}$ include only the single scattering by δv, although the infinite MS by t is taken into account. In this regard, previous calculations for bcc iron have shown that each u term yields different XMCD spectra, and neither can be neglected [12]. More explicit forms of Ξ are given as

$$\Xi^{GG}_{BL,\sigma}=m\sigma\left(\left[\xi^\sigma_B\right]^{jj}_l-4ik\left[(\xi v)^\sigma_B\right]^{jj}_l-4k^2\left[(v\xi v)^\sigma_B\right]^{jj}_l\right), \quad (A14)$$

$$\Xi^{Z'G}_{BL,\sigma}=m\sigma\left(\left[\xi^\sigma_B\right]^{Rj}_l-2ik\left[(\xi v)^\sigma_B\right]^{Rj}_l\right), \quad (A15)$$

$$\Xi^{Z'Z'}_{\alpha L,\sigma}=m\sigma\left[\xi^\sigma_\alpha\right]^{RR}_l. \quad (A16)$$

As the SOI scattering term, only the first term in $\Xi^{GG}_{BL,\sigma}$, which is the smallest in u^{GG}, was taken into account in

Ref. [11], while only $u^{Z'Z'}$ was included in Ref. [9]. These expressions, therefore, may be more comprehensive than the previous derivation. The definition and detailed contribution of the radial integral $[\cdots]$ was studied in Ref. [12]. As a result, $[v\xi v]^{jj}$, $[\xi v]^{Rj}$, and $[\xi]^{RR}$ have been observed to dominantly contribute to XMCD, while contributions from $[\xi]^{jj}$, $[\xi]^{Rj}$, and $[\xi v]^{jj}$, where ξ and j directly overlap, are quite small.

[1] B. T. Thole, P. Carra, F. Sette, and G. van der Laan, Phys. Rev. Lett. **68**, 1943 (1992).
[2] P. Carra, B. T. Thole, M. Altarelli, and X. Wang, Phys. Rev. Lett. **70**, 694 (1993).
[3] C. T. Chen, Y. U. Idzerda, H.-J. Lin, N. V. Smith, G. Meigs, E. Chaban, G. H. Ho, E. Pellegrin, and F. Sette, Phys. Rev. Lett. **75**, 152 (1995).
[4] H. Wende and C. Antoniak, *Magnetism and Synchrotron Radiation* (Springer, Heidelberg, 2010), p. 145.
[5] J. I. Igarashi and K. Hirai, Phys. Rev. B **50**, 17820 (1994).
[6] J. I. Igarashi and K. Hirai, Phys. Rev. B **53**, 6442 (1996).
[7] S. Stähler, G. Schütz, and H. Ebert, Phys. Rev. B **47**, 818 (1993).
[8] H. Ebert, Rep. Prog. Phys. **59**, 1665 (1996).
[9] C. Brouder, M. Alouani, and K. H. Bennemann, Phys. Rev. B **54**, 7334 (1996).
[10] T. Fujikawa and S. Nagamatsu, Jpn. J. Appl. Phys. **41**, 2005 (2002).
[11] T. Fujikawa and S. Nagamatsu, J. Electron Spectrosc. Relat. Phenom. **129**, 55 (2003).
[12] A. Koide, K. Niki, S. Sakai, and T. Fujikawa, J. Phys.: Conf. Ser. **712**, 012010 (2016).
[13] O. Mathon, F. Baudelet, J.-P. Itié, A. Polian, and S. Pascarelli, J. Synchrotron Radiat. **11**, 423 (2004).
[14] F. Baudelet, S. Pascarelli, O. Mathon, J. P. Itié, A. Polian, M. d'Astuto, and J. C. Chervin, J. Phys.: Condens. Matter **17**, S957 (2005).
[15] T. Koide, H. Miyauchi, J. Okamoto, T. Shidara, T. Sekine, T. Saitoh, A. Fujimori, H. Fukutani, M. Takano, and Y. Takeda, Phys. Rev. Lett. **87**, 246404 (2001).
[16] E. Goering, A. Bayer, S. Gold, S. Schütz, M. Rabe, U. Rüdiger, and G. Güntherodt, Europhys. Lett. **58**, 906 (2002).
[17] V. Kanchana, G. Vaitheeswaran, and M. Alouani, J. Phys.: Condens. Matter **18**, 5155 (2006).
[18] F. Leuenberger, A. Parge, W. Felsch, K. Fauth, and M. Hessler, Phys. Rev. B **72**, 014427 (2005).
[19] V. N. Antonov, B. N. Harmon, A. N. Yaresko, and A. P. Shpak, Phys. Rev. B **75**, 184422 (2007).
[20] V. M. Karpan, G. Giovannetti, P. A. Khomyakov, M. Talanana, A. A. Starikov, M. Zwierzycki, J. van den Brink, G. Brocks, and P. J. Kelly, Phys. Rev. Lett. **99**, 176602 (2007).
[21] M. Weser, Y. Rehder, K. Horn, M. Sicot, M. Fonin, A. B. Preobrajenski, E. N. Voloshina, E. Goering, and Y. S. Dedkov, Appl. Phys. Lett. **96**, 012504 (2010).
[22] Y. Matsumoto, S. Entani, A. Koide, M. Ohtomo, P. V. Avramov, H. Naramoto, K. Amemiya, T. Fujikawa, and S. Sakai, J. Mater. Chem. C **1**, 5533 (2013).
[23] J. J. Rehr and R. C. Albers, Rev. Mod. Phys. **72**, 621 (2000).
[24] A. Koide, T. Fujikawa, and N. Ichikuni, J. Electron Spectrosc. Relat. Phenom. **195**, 375 (2014).
[25] W. Kohn and N. Rostoker, Phys. Rev. **94**, 1111 (1954).
[26] F. M. F. de Groot, Chem. Rev. **101**, 1779 (2001).
[27] C. B. Stagarescu, X. Su, D. E. Eastman, K. N. Altmann, F. J. Himpsel, and A. Gupta, Phys. Rev. B **61**, R9233(R) (2000).
[28] D. I. Khomskii and G. A. Sawatzky, Solid State Commun. **102**, 87 (1997).
[29] M. A. Korotin, V. I. Anisimov, D. I. Khomskii, and G. A. Sawatzky, Phys. Rev. Lett. **80**, 4305 (1998).
[30] P. I. Sorantin and K. Schwarz, Inorg. Chem. **31**, 567 (1992).
[31] Y. Ji, G. J. Strijkers, F. Y. Yang, C. L. Chien, J. M. Byers, A. Anguelouch, G. Xiao, and A. Gupta, Phys. Rev. Lett. **86**, 5585 (2001).
[32] M. Sperlich, C. König, G. Güntherodt, A. Sekiyama, G. Funabashi, M. Tsunekawa, S. Imada, A. Shigemoto, K. Okada, A. Higashiya, M. Yabashi, K. Tamasaku, T. Ishikawa, V. Renken, T. Allmers, M. Donath, and S. Suga, Phys. Rev. B **87**, 235138 (2013).
[33] H. Fujiwara, M. Sunagawa, K. Terashima, T. Kittaka, T. Wakita, Y. Muraoka, and T. Yokoya, Appl. Phys. Lett. **106**, 202404 (2015).
[34] H.-T. Jeng and G. Y. Guo, J. Appl. Phys. **92**, 951 (2002).
[35] J. Kuneš, P. Novák, P. M. Oppeneer, C. König, M. Fraune, U. Rüdiger, G. Güntherodt, and C. Ambrosch-Draxl, Phys. Rev. B **65**, 165105 (2002).
[36] I. V. Solovyev, I. V. Kashin, and V. V. Mazurenko, Phys. Rev. B **92**, 144407 (2015).
[37] D. J. Huang, H.-T. Jeng, C. F. Chang, G. Y. Guo, J. Chen, W. P. Wu, S. C. Chung, S. G. Shyu, C. C. Wu, H.-J. Lin, and C. T. Chen, Phys. Rev. B **66**, 174440 (2002).
[38] M. Komelj, C. Ederer, and M. Fähnle, Phys. Rev. B **69**, 132409 (2004).
[39] H. Brändle, D. Weller, S. S. P. Parkin, J. C. Scott, P. Fumagalli, W. Reim, R. J. Gambino, R. Ruf, and G. Guntherodt, Phys. Rev. B **46**, 13889 (1992).
[40] L. Boehnke, F. Nilsson, F. Aryasetiawan, and P. Werner, Phys. Rev. B **94**, 201106 (2016).
[41] F. Gesztesy, H. Grosse, and B. Thaller, Ann. Inst. Henri Poincaré **40**, 159 (1984).
[42] O. K. Andersen and O. Jepsen, Phys. Rev. Lett. **53**, 2571 (1984).
[43] D. Taylor, Trans. J. Br. Ceram. Soc. **83**, 32 (1984).
[44] K. Hatada, K. Hayakawa, M. Benfatto, and C. R. Natoli, J. Phys.: Condens. Matter **21**, 104206 (2009).
[45] K. Hatada, K. Hayakawa, M. Benfatto, and C. R. Natoli, J. Phys.: Condens. Matter **22**, 185501 (2010).
[46] D. Sébilleau, K. Hatada, H.-F. Zhao, and C. R. Natoli, e-J. Surf. Sci. Nanotechnol. **10**, 599 (2012).
[47] M. Taillefumier, D. Cabaret, A.-M. Flank, and F. Mauri, Phys. Rev. B **66**, 195107 (2002).
[48] Y. Liang, J. Vinson, S. Pemmaraju, W. S. Drisdell, E. L. Shirley, and D. Prendergast, Phys. Rev. Lett. **118**, 096402 (2017).
[49] K. Tomita, T. Miyata, W. Olovsson, and T. Mizoguchi, Ultramicroscopy **178**, 105 (2017).